**ORIGINAL PAPER**

# Electrochemical performances of Li-rich Mn-based layered structure cathodes optimized by compositional design

Leilei Liu[1] · Guobiao Su[1] · Xu Cheng[1] · Han Han[2] · Wenjiang Qiang[1] · Bingxin Huang[1]

## Abstract

Li-rich Mn-based $xLi_2MnO_3 \cdot (1-x)LiMO_2$ (M = Ni, Co, Mn) cathode materials have attracted extensive attention because of their specific discharge capacity (250–300 mAh g$^{-1}$). However, their applications are significantly limited due to disadvantages, such as the low efficiency, the fast capacity attenuation, and the poor rate capability. Therefore, it is important to investigate the mechanisms controlling the electrochemical properties and improve the performances. As a solid solution, $xLi_2MnO_3 \cdot (1-x)LiMO_2$ is composed of the hexagonal phase $LiMO_2$ and the monoclinic phase $Li_2MnO_3$. In this study, the influence of elements Ni and Li on the electrochemical properties of $xLi_2MnO_3 \cdot (1-x)LiMO_2$ is systematically studied. It is found that the decrease of Li content can lead to the increase of $LiMO_2$ in $Li_xCo_{0.13}Ni_{0.13}Mn_{0.54}O_2$ system. $LiMO_2$ might span the whole grain with the Li deficiency, thus contributing to the rapid conduction of Li ions. Meanwhile, $Li_2MnO_3$ can benefit the structural stability. The synergistic effect of the two components results in the excellent electrochemical performances.

**Keywords** Li-rich cathode · Phase composition · Solid solution · Cycle stability · Li deficiency

## Introduction

Mobile electronics, electric vehicles, power grid energy storage, and other fields are continuously in desperate need of the lithium batteries with high energy densities, which are mainly determined by the cathode materials [1–4]. The current cathode materials such as $LiFePO_4$, $LiNi_{1-x-y}Co_xMn_yO_2$, and $LiMn_2O_4$ can no longer meet the requirements for the high energy density [5]. In contrast, Li-rich Mn-based layered oxides $xLi_2MnO_3 \cdot (1-x)LiMO_2$ (0 < x < 1, M = Mn, Co, Ni) (LLO), due to their high specific capacity, high operating voltage, and low cost [6, 7], are widely considered as potential cathode materials for the next generation of commercial lithium-ion batteries. LLO can be commonly written in two forms, either as $xLi_2MnO_3 \cdot (1-x)LiMO_2$ or as $Li_{1+x}M_{1-x}O_2$ (M = Ni, Co, Mn) [8, 9], which can easily reflect the phase

compositions or total elemental compositions, respectively. In terms of phase compositions, LLO consists of two layered structures $LiMO_2$ and $Li_2MnO_3$ (Fig. 1). $LiMO_2$ has a hexagonal α-NaFeO$_2$ structure with a space group $R\bar{3}m$, and the transition atoms randomly distribute in M layers (Fig. 1a). $Li_2MnO_3$ has a similar layered structure as α-NaFeO$_2$. The difference lies in that one layer in $Li_2MnO_3$ is completely occupied by Li, while the other layer is occupied by 1/3 Li and 2/3 Mn (Fig. 1b). As a result, the chemical formula of $Li_2MnO_3$ can also be written as $Li[Li_{1/3}Mn_{2/3}]O_2$. Because of the mixed layer of Li and Mn, $Li_2MnO_3$ belongs to the monoclinic system with a space group $C2/m$.

Since $LiMO_2$ and $Li_2MnO_3$ have the similar layered structure and interlayer spacing, the crystal structure of LLO is difficult to be accurately characterized. Based on the experimental results, LLO is considered to be a solid solution of $LiMO_2$ and $Li_2MnO_3$ [10–14], and the lattice parameters depend linearly on the composition and follow Vegard's principle [11, 15–17]. The intergrowth of two-phase domains has been directly observed in LLO, and therefore, a nanocomposite structure of $LiMO_2$ phase and $Li_2MnO_3$ phase is proposed for LLO [8, 13, 18–23]. Until now, there is still no clear conclusion about the structure of LLO [24]. A schematic illustration of the structure using two color balls as shown in Fig. 2 aims to clearly describe the

✉ Han Han
  Han.Han@imec.be

✉ Bingxin Huang
  bxhuang@ustb.edu.cn

1  Shunde Graduate School of University of Science and Technology, Beijing, Foshan 528399, China

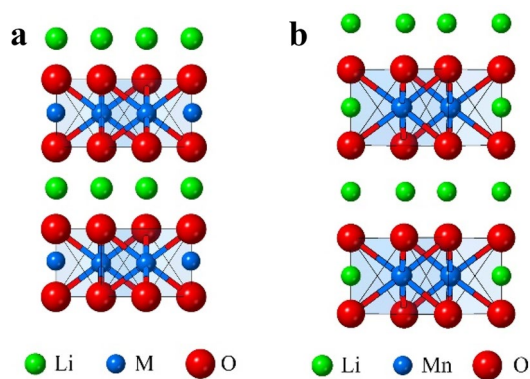2  Interuniversity Microelectronics Centre (Imec), 3001 Louvain, Belgium

Fig. 1 **a**, **b** Schematic illustration of layered crystal structures of $LiMO_2$ and $Li_2MnO_3$

situation. The zero-interaction energy between the balls indicates a completely random distribution of the balls, which can in a way reflect the atom distribution in an ideal binary solution. The clusters are dominant in ideal solutions, and each cluster contains dozens or even more atoms. The clusters are consistent with the observed intergrowth two-phase domains [20, 25]. Therefore, it can be inferred that LLO is a solid solution of $LiMO_2$ and $Li_2MnO_3$.

The high specific capacity of LLO originates from both cationic redox (M ions) in $LiMO_2$ and anionic (O ions)



Fig. 2 The visual exhibition of $LiMO_2$ and $Li_2MnO_3$ clusters in ideal solution in LLO

redox in $Li_2MnO_3$ [26, 27]. On the other hand, the oxygen redox gives rise to the irreversible oxygen loss, thus leading to a low coulomb efficiency of the first cycle [27, 28]. Moreover, the serious attenuations of capacity and voltage, and poor rate capability inhibit the application of LLO. Such unwanted electrochemical performances of LLO can be improved by applying nanoparticles, bulk doping, and surface coating [29–33]. Furthermore, the oxygen loss in $Li_2MnO_3$ and electrochemical performances are significantly determined by the chemical compositions of the $LiMO_2$-$Li_2MnO_3$ solid solutions [5, 14, 34, 35].

In this study, different experiments have been designed and a variety of characterization methods have been applied to study the factors that can affect the oxygen loss in LLO as well as the subsequent capacity. Moreover, the chemical compositions of Ni and Li have been fine tuned to optimize the electrochemical performances.

## Experiments

A mixed salt solution is prepared with an appropriate amount of $MnSO_4·H_2O$, $NiSO_4·6H_2O$, and $CoSO_4·7H_2O$. A $Na_2CO_3$ solution is prepared separately. The two solutions are simultaneously dripped into the reactor with a peristaltic pump. During the reaction, $NH_4·OH$ is used as a complexing agent and a pH regulator in the reaction. After the reaction, the product is washed several times, and the carbonate precursor $Ni_xCo_{0.26-x}Mn_{0.54}(CO_3)_{0.8}$ is obtained. The prepared carbonate precursor and $LiOH·H_2O$ are fully mixed in a mortar. Considering the Li loss during the sintering process, an excess of 3% Li is added. The mixed powder is pre-sintered at 500 ℃ for 5 h (h), and then sintered at 850 ℃ for 15 h. Li-rich and Mn-based cathode materials $Li_{1.2}Co_{0.26-x}Ni_xMn_{0.54}O_2$ and $Li_xMn_{0.54}Ni_{0.13}Co_{0.13}O_2$ are obtained. The whole sintering process is carried out in oxygen atmosphere.

CR2032 coin cells are assembled to study the electrochemical properties of the cathodes. The active material, polyvinylidene fluoride (PVDF), and acetylene black (AB) are blended according to the mass ratio of 8:1:1, and the loading amount of the active material in the electrode is 2.5–3 mg cm$^{-2}$. A Li metal sheet is used as a negative electrode. The diaphragm is Celgard 2300, and the electrolyte is $LiPF_6$ dissolved in ethyl carbonate (EC). The electrochemical performance is investigated with the cell test system (Land CT2001A) in the voltage window of 2.0–4.8 V (1C = 250 mAh g$^{-1}$), and all experiments are carried out at 25 ℃. Electrochemical impedance spectra (EIS) are analyzed in the frequency range of $10^{-2}$–$10^5$ Hz using an electrochemical workstation (Autolab, PGSTAT302N),

and the cells are charged to 4.0 V before testing the impedance. The cyclic voltammetry (CV) curves between 2 and 4.8 V are measured with the electrochemical workstation. The crystal structure is investigated by X-ray diffraction (XRD, Ultima IV, RIGAKU Corporation). The morphology and size of cathode particles are characterized by field emission scanning electron microscopy (SEM, gemini500, Zeiss). The microstructure and phase composition are characterized by high-resolution transmission electron microscopy (HR-TEM).

## Results and discussions

The morphologies of the precursor and cathode particles are presented in Fig. 3. The surface of $Co_{0.26}Mn_{0.54}(CO_3)_{0.8}$ particle is smooth, and the particle size is 6–10 μm. With the addition of Ni, fine debris are adhered to the surface of precursor particles. The spherical particles of $Co_{0.26}Mn_{0.54}(CO_3)_{0.8}$ are inherited for $Li_{1.2}Co_{0.26}Mn_{0.54}O_2$, and the cathode particles are dense. However, the particles of $Li_{1.2}Co_{0.26-x}Ni_xMn_{0.54}O_2$

**Fig. 3** SEM images of $Co_{0.26-x}Ni_xMn_{0.54}(CO_3)_{0.8}$ precursors and $Li_{1.2}Co_{0.26-x}Ni_xMn_{0.54}O_2$ cathodes. (**a**) $Co_{0.26}Mn_{0.54}(CO_3)_{0.8}$, (**b**) $Co_{0.195}Ni_{0.065}Mn_{0.54}(CO_3)_{0.8}$, (**c**) $Co_{0.13}Ni_{0.13}Mn_{0.54}(CO_3)_{0.8}$, (**d**) $Co_{0.065}Ni_{0.195}Mn_{0.54}(CO_3)_{0.8}$, (**e**) $Li_{1.2}Co_{0.26}Mn_{0.54}O_2$, (**f**) $Li_{1.2}Co_{0.195}Ni_{0.065}Mn_{0.54}O_2$, (**g**) $Li_{1.2}Co_{0.13}Ni_{0.13}Mn_{0.54}O_2$, (**h**) $Li_{1.2}Co_{0.065}Ni_{0.195}Mn_{0.54}O_2$
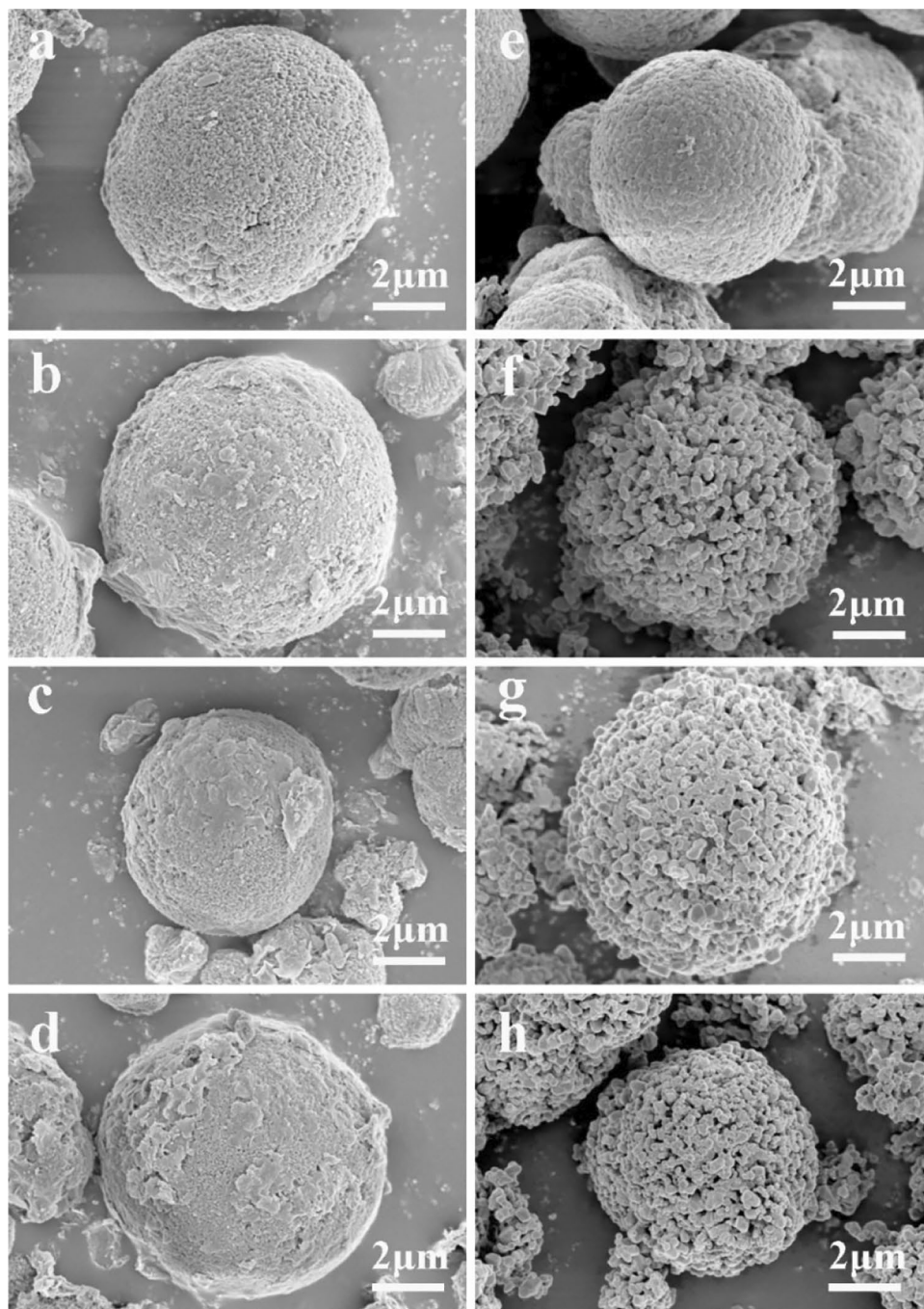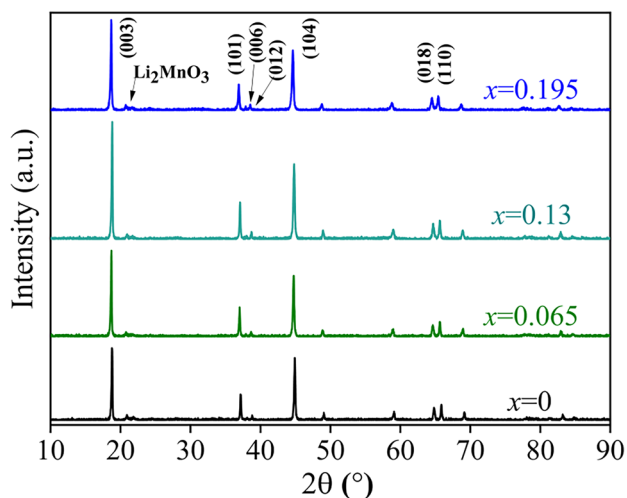
**Fig. 4** XRD patterns of $Li_{1.2}Co_{0.26-x}Ni_xMn_{0.54}O_2$ (x = 0, 0.065, 0.13, 0.195)

(x = 0.065, 0.13, 0.195) are porous, and they have a similar morphology independence of Ni content, which could be ascribed to that Ni hinders the densification during sintering.

The XRD patterns of $Li_{1.2}Co_{0.26-x}Ni_xMn_{0.54}O_2$ are plotted in Fig. 4. Because the crystal structures of $LiMO_2$ and $Li_2MnO_3$ are very similar, their XRD patterns are almost identical. The only difference is the small characteristic peak of $Li_2MnO_3$ at 20–25°. Therefore, all samples are indexed as $Li_2MnO_3$ phase or the mixture of hexagonal $LiMO_2$

phase and monoclinic $Li_2MnO_3$ phase [36–38]. The lattice constants a and c increase continuously with the Ni content, which could be attributed to the larger radius of $Ni^{2+}$ (0.69 Å) compared to that of $Co^{3+}$ (0.55 Å) [39]. The ratios of c/a and I(003)/I(104) reflect the degree of the cation mixing, and a higher value indicates a lower cation mixing [40, 41]. The ratios of both c/a and I(003)/I(104) decrease with the Ni content, suggesting that Ni results in cation mixing due to the similar ionic radius of $Li^+$ and $Ni^{2+}$ [39].

The cycle stability of the samples is measured in the range of 2.0–4.8 V. The current of the first three cycles is 0.1 C, and the current of the following cycles is 0.5 C. The initial charge–discharge curves of $Li_{1.2}Co_{0.26-x}Ni_xMn_{0.54}O_2$ are shown in Fig. 5a. All curves consist of two stages. The first stage between 3.9 and 4.5 V is mainly due to the redox of $Ni^{2+}$ and $Co^{3+}$ into high valence states. The second stage at about 4.5 V is mainly related to the reduction of $O^{2-}$ to O, and this process is partially reversible, resulting in a low first coulomb efficiency. The initial discharge capacity of $Li_{1.2}Co_{0.26-x}Ni_xMn_{0.54}O_2$ is 38.1 mAh g$^{-1}$, 165.8 mAh g$^{-1}$, 187 mAh g$^{-1}$, and 162.6 mAh g$^{-1}$ for x = 0, 0.065, 0.13, and 0.195, respectively. With the increase of Ni content, the discharge capacity first increases and then decreases, and $Li_{1.2}Co_{0.13}Ni_{0.13}Mn_{0.54}O_2$ has the highest capacity. The capacity retention rates are 73.7%, 85.8%, and 93.9% for x = 0.065, 0.13, and 0.195, respectively (Fig. 5b). The medium voltage of $Li_{1.2}Co_{0.26-x}Ni_xMn_{0.54}O_2$, presented in Fig. 5c, increases with the Ni content. With the increase

**Fig. 5** Electrochemical performances of $Li_{1.2}Co_{0.26-x}Ni_xMn_{0.54}O_2$ (x = 0, 0.065, 0.13, 0.195). (**a**) The initial charge–discharge curves. (**b**) Cycle stability. (**c**) Medium voltage
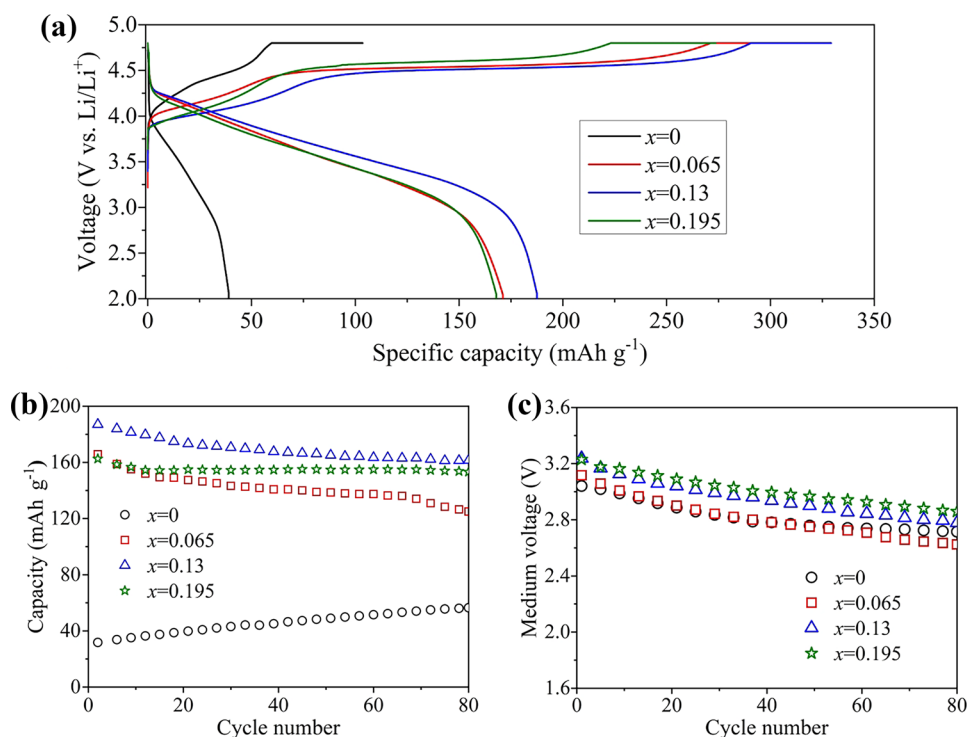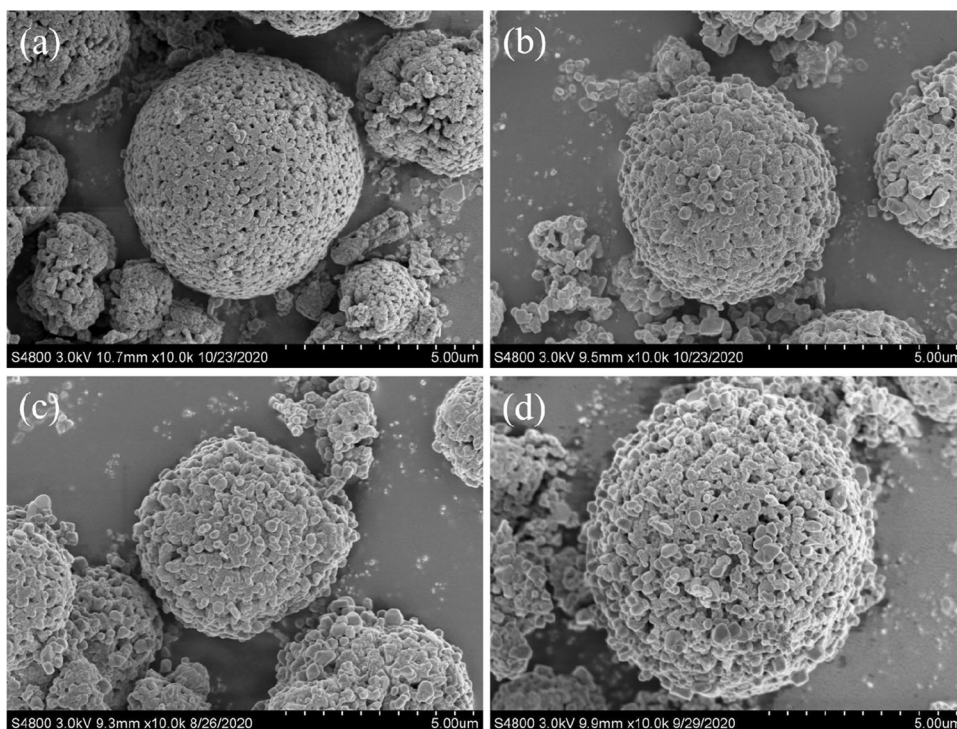
**Fig. 6** SEM images of
$Li_xCo_{0.13}Ni_{0.13}Mn_{0.54}O_2$
with varying Li contents:
(**a**) x = 1.02, (**b**) x = 1.08, (**c**)
x = 1.14, (**d**) x = 1.2



of Ni content, the voltage attenuation decreases. High Co content can lead to the formation of well-defined hexagonal layered structures, and thus better electrochemical performances. On the other hand, high Co content can reduce the $Ni^{2+}/Ni^{4+}$ redox pair, which is not conducive to the electrochemical performances [42–44]. Therefore, an appropriate Ni content gives the best electrochemical performances.

$Li_{1.2}Co_{0.13}Ni_{0.13}Mn_{0.54}O_2$ has the best electrochemical performances in $Li_{1.2}Co_{0.26-x}Ni_xMn_{0.54}O_2$ series. Therefore, $Li_xCo_{0.13}Ni_{0.13}Mn_{0.54}O_2$ (x = 1.2, 1.14, 1.08, 1.02) is investigated further to study the effect of Li content on electrochemical performances. The SEM pictures of $Li_xCo_{0.13}Ni_{0.13}Mn_{0.54}O_2$ are presented in Fig. 6. All samples are spherical secondary particles composed of primary particles. The particles of all samples are porous and comparable with each other, implying that the morphology is not significantly affected by the Li content. The XRD patterns of $Li_xCo_{0.13}Ni_{0.13}Mn_{0.54}O_2$ are similar for all x values (Fig. 7), which could be indexed as α-NaFeO$_2$ structure (space group: R$\bar{3}$m). The small peak between 20 and 25° represents $Li_2MnO_3$ with monoclinic structure (C2/M space group).

The structures of $Li_{1.02}Co_{0.13}Ni_{0.13}Mn_{0.54}O_2$ and $Li_{1.2}Co_{0.13}Ni_{0.13}Mn_{0.54}O_2$ samples are further analyzed using HR-TEM and fast Fourier transformation (FFT) (Fig. 8). An example HR-TEM image of $Li_{1.2}Co_{0.13}Ni_{0.13}Mn_{0.54}O_2$ is shown in Fig. 8a. The region in the red square is further magnified in Fig. 8b with the zone axis of [010], confirmed by FFT analysis. The determined lattice plane spacing as

marked in Fig. 8b is ~ 0.43 nm, which corresponds to the (020) plane of the monoclinic C2/m structure, indicating more $Li_2MnO_3$ phase in the $Li_{1.2}Co_{0.13}Ni_{0.13}Mn_{0.54}O_2$ sample. Similarly, one example HR-TEM image of $Li_{1.02}Co_{0.13}Ni_{0.13}Mn_{0.54}O_2$ is shown in Fig. 8c and the magnified image of the region in the red square is presented in Fig. 8d. The investigated region has a hexagonal R$\bar{3}$m structure determined from FFT image. The determined lattice plane spacing in Fig. 8d is ~ 0.47 nm, which agrees well with the (003) planes of the R$\bar{3}$m structure. Another
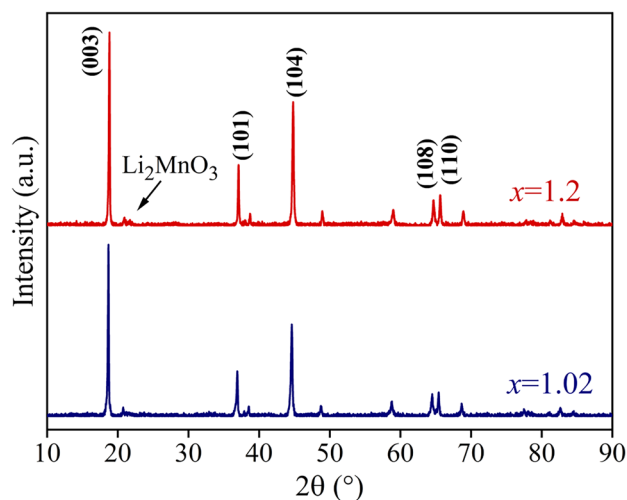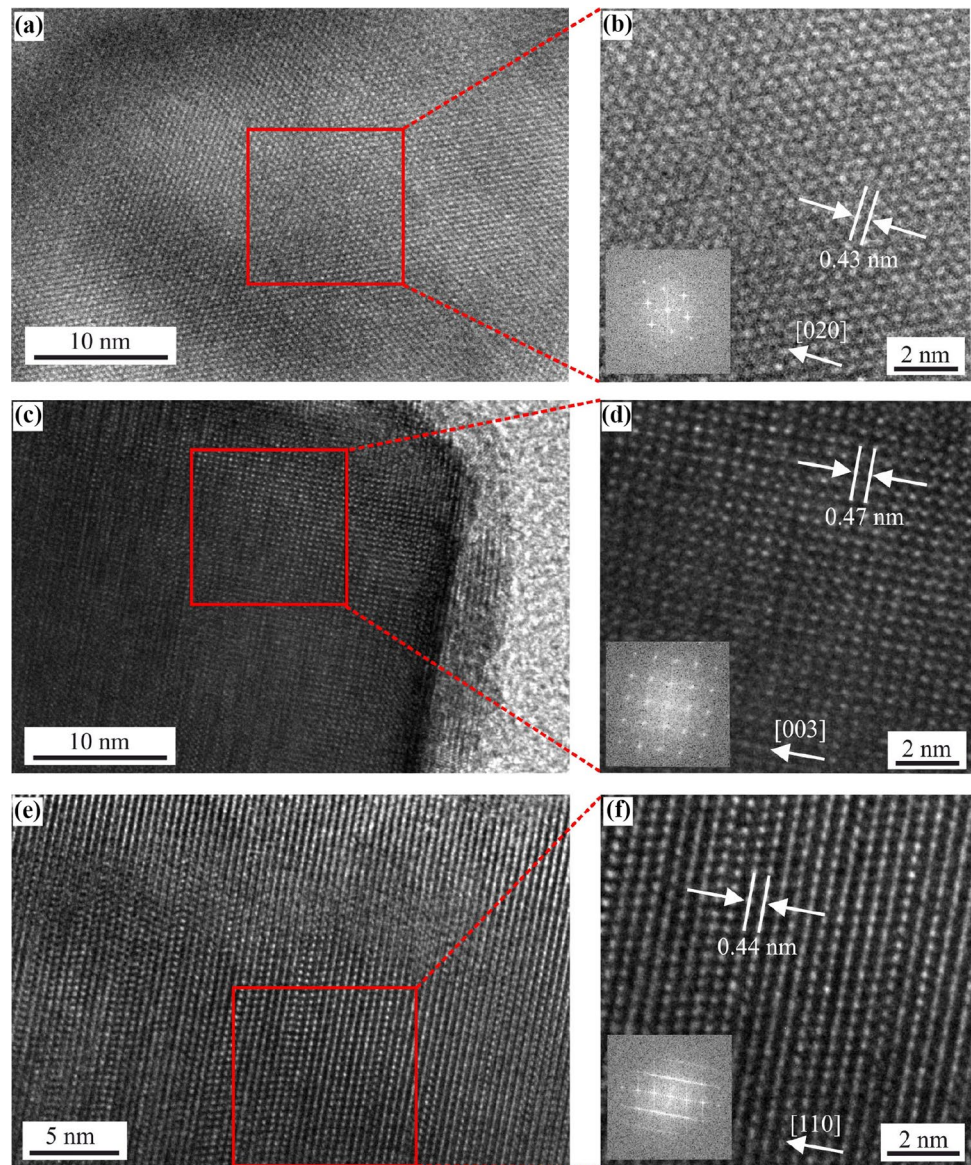


**Fig. 7** XRD patterns of $Li_xCo_{0.13}Ni_{0.13}Mn_{0.54}O_2$ (x = 1.02, 1.2)

**Fig. 8** (**a**) HR-TEM image of Li1.2 and marked region of (**a**) is further magnified in (**b**), (**c**) HR-TEM image of Li1.02 and marked region of (**c**) is further magnified in (**d**), (**e**) HR-TEM image of Li1.02 and marked region of (**e**) is further magnified in (**f**). The insets in (**b**), (**d**), and (**f**) show the corresponding fast Fourier transformation of the marked regions



example HR-TEM image of $Li_{1.02}Co_{0.13}Ni_{0.13}Mn_{0.54}O_2$ showing the monoclinic C2/m structure with the zone axis of (110) is shown in Fig. 8f, magnified further from Fig. 8e. The determined lattice plane spacing in Fig. 8f is ~0.44 nm, which corresponds to the (110) planes of the monoclinic C2/m structure. The theoretical phase compositions of $Li_{1.2}Co_{0.13}Ni_{0.13}Mn_{0.54}O_2$ are 60% $Li_{4/3}Mn_{2/3}O_2$ (monoclinic) and 40% $LiNi_{1/3}Co_{1/3}Mn_{1/3}O_2$, and the theoretical phase compositions of $Li_{1.02}Co_{0.13}Ni_{0.13}Mn_{0.54}O_2$ are 36% $Li_{4/3}Mn_{2/3}O_2$ and 64% $LiNi_{0.224}Co_{0.224}Mn_{0.552}O_2$ (hexagonal), which is consistent with the TEM observations. Although many literatures have reported that the spinel phase can be formed by lithium deficiencies [45–47], no spinel phase has been identified in the $Li_{1.02}Co_{0.13}Ni_{0.13}Mn_{0.54}O_2$ sample. This is probably due to the limited sampling regions

of TEM, and the possibility of the existence of spinel phase cannot be ruled out.

The cycle stability of $Li_xCo_{0.13}Ni_{0.13}Mn_{0.54}O_2$ at 0.5 C is shown in Fig. 9a. The initial specific capacities of $Li_xCo_{0.13}Ni_{0.13}Mn_{0.54}O_2$ are 212.0 mAh g$^{-1}$, 224.8 mAh g$^{-1}$, 202.0 mAh g$^{-1}$, and 187.0 mAh g$^{-1}$ for x = 1.02, 1.08, 1.14, and 1.2, respectively. In general, the electrochemical performances of $Li_xCo_{0.13}Ni_{0.13}Mn_{0.54}O_2$ increase with the decrease of Li content. $Li_{1.08}Co_{0.13}Ni_{0.13}Mn_{0.54}O_2$ exhibits the highest initial capacity, and $Li_{1.02}Co_{0.13}Ni_{0.13}Mn_{0.54}O_2$ delivers the best cycle stability with a capacity retention of 100.5% after 200 cycles. The excellent electrochemical properties of $Li_{1.02}Co_{0.13}Ni_{0.13}Mn_{0.54}O_2$ may be related to its phase compositions. With the decrease of Li content, the ratio of $LiMO_2$ phase increases and $Li_{4/3}Mn_{2/3}O_2$ phase decreases, as proved by TEM

**Fig. 9** Electrochemical performances of $Li_xCo_{0.13}Ni_{0.13}Mn_{0.54}O_2$. (**a**) Cycle stability. (**b**) Medium voltage. (**c**) Typical charge/discharge curves of $Li_{1.2}Co_{0.13}Ni_{0.13}Mn_{0.54}O_2$. (**d**) Typical charge/discharge curves of $Li_{1.2}Co_{0.13}Ni_{0.13}Mn_{0.54}O_2$
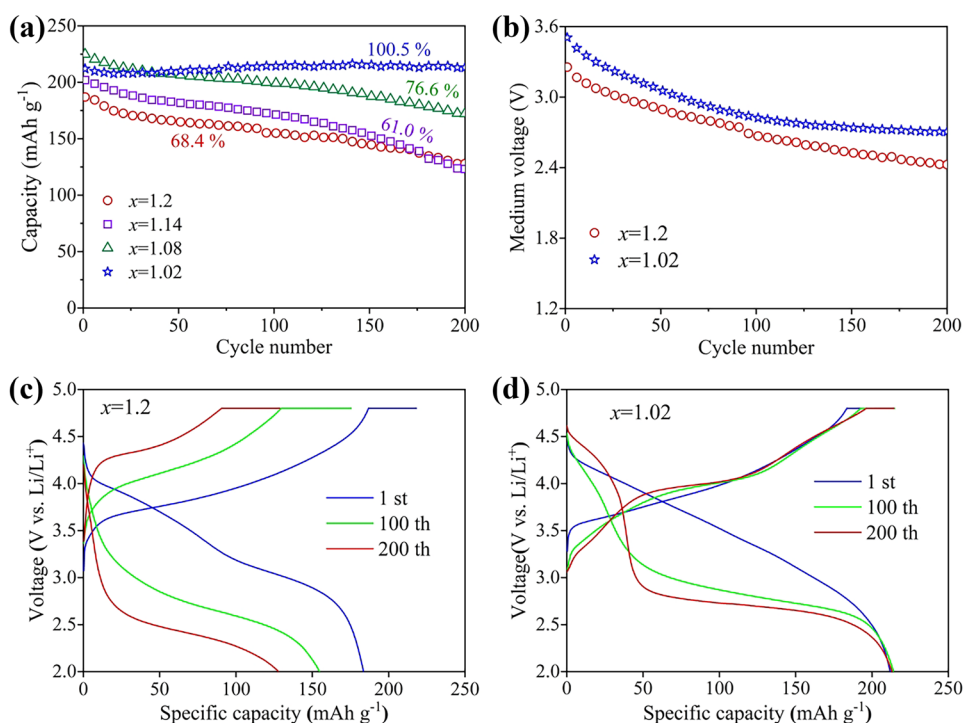


(Fig. 8). As a solid solution, the hexagonal phase $LiMO_2$ could span the whole grain in $Li_{1.02}Co_{0.13}Ni_{0.13}Mn_{0.54}O_2$, which is conducive to the conduction of Li ions. At the same time, the monoclinic phase $Li_{4/3}Mn_{2/3}O_2$ can maintain the structural stability. Therefore, the synergistic effect of the two phases can give rise to the high capacity and cycle stability. The discharge medium voltage of $Li_{1.02}Co_{0.13}Ni_{0.13}Mn_{0.54}O_2$ is always higher than that of $Li_{1.2}Co_{0.13}Ni_{0.13}Mn_{0.54}O_2$ (Fig. 9b). The discharge capacity and voltage of $Li_{1.2}Co_{0.13}Ni_{0.13}Mn_{0.54}O_2$ decrease continuously with the cycles (Fig. 9c), while $Li_{1.2}Co_{0.13}Ni_{0.13}Mn_{0.54}O_2$ could maintain the voltage stability (Fig. 9d).

**Fig. 10** Electrochemical analysis of $Li_xCo_{0.13}Ni_{0.13}Mn_{0.54}O_2$: (**a**) CV curves of $Li_{1.2}Co_{0.13}Ni_{0.13}Mn_{0.54}O_2$, (**b**) CV curves of $Li_{1.02}Co_{0.13}Ni_{0.13}Mn_{0.54}O_2$, (**c**) EIS at the 1st cycle, (**d**) EIS at the 50th cycle
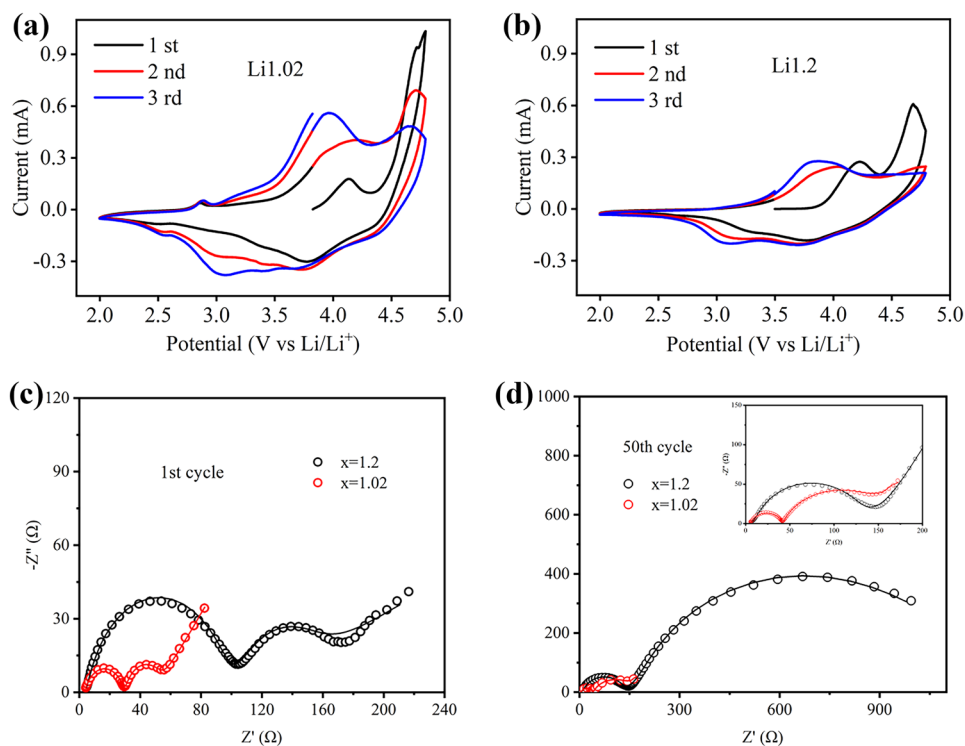
**Table 1** Resistance of $Li_xCo_{0.13}Ni_{0.13}Mn_{0.54}O_2$

| Samples | 1st | | | 50th | | |
|---|---|---|---|---|---|---|
| | $R_s/\Omega$ | $R_{SEI}/\Omega$ | $R_{ct}/\Omega$ | $R_s/\Omega$ | $R_{SEI}/\Omega$ | $R_{ct}/\Omega$ |
| $Li_{1.2}Ni_{0.13}Co_{0.13}Mn_{0.54}O_2$ | 2.3 | 84.7 | 32.6 | 7.0 | 142.9 | 1120.0 |
| $Li_{1.02}Ni_{0.13}Co_{0.13}Mn_{0.54}O_2$ | 3.5 | 23.8 | 16.2 | 5.2 | 35.5 | 156.4 |

To explore the transition process of $Li_xCo_{0.13}Ni_{0.13}Mn_{0.54}O_2$ (x = 1.2, 1.02) during cycles, the CV curves of two samples are studied (Fig. 10a and b). Both samples exhibit a small peak at ~4.1 V and a large peak at ~4.7 V, which correspond to the activation of $LiMO_2$ and $Li_2MnO_3$ components, respectively. After the second cycle, the activation peak of $Li_2MnO_3$ component in x = 1.2 is quite weak while the activation peak of $Li_2MnO_3$ component in x = 1.02 is still strong, indicating a better reversibility of $Li_{1.02}Co_{0.13}Ni_{0.13}Mn_{0.54}O_2$. The electrochemical impedance spectra of the first and 50th cycles were measured, and the Nyquist plots are shown in Fig. 10c and d. Both curves are composed of two semicircles and a straight line. The semicircle in the high frequency region is related to the resistance of the SEI film, and the semicircle in the medium frequency region is related to the charge transfer process between the positive material and the electrolyte, and the straight line in the low frequency region results from the Warburg diffusion process in bulk materials [48–50]. The resistance values are listed in Table 1. In the first cycle, the $R_{SEI}$ and $R_{ct}$ of $Li_{1.02}Co_{0.13}Ni_{0.13}Mn_{0.54}O_2$ were significantly lower than those of $Li_{1.2}Co_{0.13}Ni_{0.13}Mn_{0.54}O_2$. After 50 cycles, $R_{SEI}$ and $R_{ct}$ of $Li_{1.2}Co_{0.13}Ni_{0.13}Mn_{0.54}O_2$ increase dramatically, while the resistance increase of $Li_{1.02}Co_{0.13}Ni_{0.13}Mn_{0.54}O_2$ is much smaller, indicating the high stability of $Li_{1.02}Co_{0.13}Ni_{0.13}Mn_{0.54}O_2$.

## Conclusions

LLO can be considered as a solid solution of $LiMO_2$ and $Li_2MnO_3$. The influences of the chemical compositions, e.g., Ni and Li in LLO, have been systematically studied in order to optimize the electrochemical performances. In $Li_{1.2}Co_{0.26-x}Ni_xMn_{0.54}O_2$ system, $Li_{1.2}Co_{0.13}Ni_{0.13}Mn_{0.54}O_2$ presents the highest capacity and the best cycle stability. Then the Ni content is fixed at 0.13, and the influence of Li contents has been further explored. We have found that the fraction of $LiMO_2$ in $Li_xCo_{0.13}Ni_{0.13}Mn_{0.54}O_2$ increases with the decrease of Li. $LiMO_2$ component can span the LLO particle, which is beneficial for the conduction of Li ions. Meanwhile, $Li_2MnO_3$ component can sustain the layered structure of $LiMnO_2$. As a result, $Li_{1.02}Co_{0.13}Ni_{0.13}Mn_{0.54}O_2$ exhibits an initial capacity of 224.8 mAh g$^{-1}$ and a capacity retention rate of 100.5% after 200 cycles.

## References

1. Goodenough JB (2018) How we made the Li-ion rechargeable battery. Nat Electron 1(3):204–204
2. Obama B (2017) The irreversible momentum of clean energy. Science 355(6321):126–129
3. Yuxuan Z, Biao L, Ning J, Wangsheng C, Hao Z, Ruqiang Z, Dingguo X (2018) A high-capacity O2-type Li-rich cathode material with a single-layer $Li_2MnO_3$ superstructure. Adv Mater 30(16):1707255
4. Kraytsberg A, Ein-Eli Y (2012) Higher, stronger, better… a review of 5 volt cathode materials for advanced lithium-ion batteries. Adv Energy Mater 2(8):922–939
5. Yin C, Wan LY, Qiu B, Wang F, Jiang W, Cui HF, Bai JM, Ehrlich S, Wei ZN, Liu ZP (2021) Boosting energy efficiency of Li-rich layered oxide cathodes by tuning oxygen redox kinetics and reversibility. Energy Storage Mater 35:388–399
6. Lu Z, MacNeil D, Dahn J (2001) Layered cathode materials $Li[Ni_xLi_{(1/3-2x/3)}Mn_{(2/3-x/3)}]O_2$ for lithium-ion batteries. Electrochem Solid-State Lett 4(11):A191–A194
7. Zuo Y, Li B, Jiang N, Chu W, Zhang H, Zou R, Xia D (2018) A high-capacity O2-type Li-rich cathode material with a single-layer $Li_2MnO_3$ superstructure. Adv Mater 30(16):1707255
8. Kim J-S, Johnson CS, Vaughey JT, Thackeray MM, Hackney SA, Yoon W, Grey CP (2004) Electrochemical and structural properties of $xLi_2MO_3(1-x)LiMn_{0.5}Ni_{0.5}O_2$ electrodes for lithium batteries (M '= Ti, Mn, Zr; 0≤ x☒ 0.3). Chem Mater 16(10):1996–2006
9. Thackeray M, Kang S-H, Johnson C, Vaughey J, Hackney S (2006) Comments on the structural complexity of lithium-rich $Li_{1+x}M_{1-x}O_2$ electrodes (M= Mn, Ni, Co) for lithium batteries. Electrochem Commun 8(9):1531–1538
10. Genevois C, Koga H, Croguennec L, Ménétrier M, Delmas C, Weill F (2015) Insight into the atomic structure of cycled lithium-rich layered oxide $Li_{1.20}Mn_{0.54}Co_{0.13}Ni_{0.13}O_2$ using HAADF STEM and electron nanodiffraction. J Phys Chem C 119(1):75–83
11. Jarvis KA, Deng Z, Allard LF, Manthiram A, Ferreira PJ (2011) Atomic structure of a lithium-rich layered oxide material for lithium-ion batteries: evidence of a solid solution. Chem Mater 23(16):3614–3621
12. Lu Z, Chen Z, Dahn J (2003) Lack of cation clustering in $Li[Ni_xLi_{1/3-x/3}Mn_{2/3-x/3}]O_2$ (0< x ≤ 1/2) and $Li[Cr_xLi_{(1-x)/3}Mn_{(2-2x)/3}]O_2$ (0< x< 1). Chem Mater 15(16):3214–3220
13. Thackeray MM, Kang S-H, Johnson CS, Vaughey JT, Benedek R, Hackney SA (2007) $Li_2MnO_3$-stabilized $LiMO_2$ (M = Mn, Ni, Co) electrodes for lithium-ion batteries. J Mater Chem 17(30):3112–3125
14. Arunkumar TA, Wu Y, Manthiram A (2007) Factors influencing the irreversible oxygen loss and reversible capacity in layered $Li[Li_{1/3}Mn_{2/3}]O_2 - Li[M]O_2$ (M = $Mn_{0.5-y}Ni_{0.5-y}Co_{2y}$ and $Ni_{1-y}Co_y$) solid solutions. Chem Mater 19(12):3067–3073

15. Ammundsen B, Paulsen J, Davidson I, Liu RS, Shen CH, Chen JM, Jang LY, Lee JF (2002) Local structure and first cycle redox mechanism of layered $Li_{1.2}Cr_{0.4}Mn_{0.4}O_2$ cathode material. J Electrochem Soc 149(4):A431-A436

16. Koga H, Croguennec L, Mannessiez P, Menetrier M, Weill F, Bourgeois L, Duttine M, Suard E, Delmas C (2012) $Li_{1.20}Mn_{0.54}Co_{0.13}Ni_{0.13}O_2$ with different particle sizes as attractive positive electrode materials for lithium-ion batteries: insights into their structure. J Phys Chem C 116(25):13497–13506

17. Ohzuku T, Nagayama M, Tsuji K, Ariyoshi K (2011) High-capacity lithium insertion materials of lithium nickel manganese oxides for advanced lithium-ion batteries: toward rechargeable capacity more than 300 mA h g$^{-1}$. J Mater Chem 21(27):10179–10188

18. Yu H, So Y-G, Kuwabara A, Tochigi E, Shibata N, Kudo T, Zhou H, Ikuhara Y (2016) Crystalline grain interior configuration affects lithium migration kinetics in Li-rich layered oxide. Nano Lett 16(5):2907–2915

19. Gu M, Genc A, Belharouak I, Wang D, Amine K, Thevuthasan S, Baer DR, Zhang J-G, Browning ND, Liu J (2013) Nanoscale phase separation, cation ordering, and surface chemistry in pristine $Li_{1.2}Ni_{0.2}Mn_{0.6}O_2$ for Li-ion batteries. Chem Mater 25(11):2319–2326

20. Yu H, Ishikawa R, So Y-G, Shibata N, Kudo T, Zhou H, Ikuhara Y (2013) Direct atomic-resolution observation of two phases in the $Li_{1.2}Mn_{0.567}Ni_{0.166}Co_{0.067}O_2$ cathode material for lithium-ion batteries. Angewandte Chemie 125(23):6085–6089

21. Thackeray MM, Johnson CS, Vaughey JT, Li N, Hackney SA (2005) Advances in manganese-oxide 'composite' electrodes for lithium-ion batteries. J Mater Chem 15(23):2257–2267

22. Johnson CS, Kim JS, Lefief C, Li N, Vaughey JT, Thackeray MM (2004) The significance of the $Li_2MnO_3$ component in 'composite' $xLi_2MnO_3·(1-x)LiMn_{0.5}Ni_{0.5}O_2$ electrodes. Electrochem Commun 6(10):1085–1091

23. Gu M, Belharouak I, Zheng JM, Wu HM, Xiao J, Genc A, Amine K, Thevuthasan S, Baer DR, Zhang JG, Browning ND, Liu J, Wang CM (2013) Formation of the spinel phase in the layered composite cathode used in Li-ion batteries. ACS Nano 7(1):760–767

24. Zhu Z, Yu D, Yang Y, Su C, Huang Y, Dong Y, Waluyo I, Wang B, Hunt A, Yao X, Lee J, Xue W, Li J (2019) Gradient Li-rich oxide cathode particles immunized against oxygen release by a molten salt treatment. Nat Energy 4(12):1049–1058

25. Yu H, Ishikawa R, So YG, Shibata N, Kudo T, Zhou H, Ikuhara Y (2013) Direct atomic-resolution observation of two phases in the $Li_{1.2}Mn_{0.567}Ni_{0.166}Co_{0.067}O_2$ cathode material for lithium-ion batteries. Angew Chem Int Ed Engl 52(23):5969–73

26. Zhang H, Omenya F, Yan P, Luo L, Whittingham MS, Wang C, Zhou G (2017) Rock-salt growth-induced (003) cracking in a layered positive electrode for Li-ion batteries. ACS Energy Lett 2(11):2607–2615

27. Wang T, Zhang C, Li S, Shen X, Zhou L, Huang Q, Liang C, Wang Z, Wang X, Wei W (2021) Regulating anion redox and cation migration to enhance the structural stability of Li-rich layered oxides. ACS Appl Mater Interfaces 13(10):12159–12168

28. Qiu B, Zhang M, Wu L, Wang J, Xia Y, Qian D, Liu H, Hy S, Chen Y, An K, Zhu Y, Liu Z, Meng YS (2016) Gas–solid interfacial modification of oxygen activity in layered oxide cathodes for lithium-ion batteries. Nat Commun 7:12108

29. Wang Z, Cheng X, Qiang W, Huang B (2019) Surface modification of Li rich $Li_{1.2}Mn_{0.54}Ni_{0.13}Co_{0.13}O_2$ cathode particles. Ceram Int 45(16):20016-20021

30. Shen Z, Li D, Tang Y, Li C (2018) Effects of $Gd^{3+}$ doping on the microstructure and electrochemical properties of $Li_{1.20}[Mn_{0.54}Ni_{0.13}Co_{0.13}]O_2$ as cathode for lithium-ion batteries. J Mater Sci: Mater Electron 29(11):9717–9727

31. Lu Y, Shi S, Yang F, Zhang T, Niu H, Wang T (2018) Mo-doping for improving the $ZrF_4$ coated-$Li[Li_{0.20}Mn_{0.54}Ni_{0.13}Co_{0.13}]O_2$ as high performance cathode materials in lithium-ion batteries. J Alloys Comp 767:23–33

32. Zhou H, Yang Z, Yin C, Yang S, Li J (2018) Fabrication of nano-plate Li-rich cathode material via surfactant-assisted hydrothermal method for lithium-ion batteries. Ceram Int 44(16):20514–20523

33. He H, Zan L, Liu J, Zhang Y (2020) Template-assisted molten-salt synthesis of hierarchical lithium-rich layered oxide nanowires as high-rate and long-cycling cathode materials. Electrochim Acta 333:135558

34. Jarvis KA, Wang C-C, Manthiram A, Ferreira PJ (2014) The role of composition in the atomic structure, oxygen loss, and capacity of layered Li–Mn–Ni oxide cathodes. Journal of Materials Chemistry A 2(5):1353–1362

35. Konishi H, Hirano T, Takamatsu D, Gunji A, Feng X, Furutsuki S (2015) Effect of composition of transition metals on stability of charged Li-rich layer-structured cathodes, $Li_{1.2}Ni_{0.2-x}Mn_{0.6-x}Co_{2x}O_2$ (x=0, 0.033, and 0.067), at high temperatures. Electrochim Acta 186:591–597

36. Kim JH, Park CW, Sun YK (2003) Synthesis and electrochemical behavior of $Li[Li_{0.1}Ni_{0.35-x/2}Co_xMn_{0.55-x/2}]O_2$ cathode materials. Solid State Ion 164(1):43–49

37. Meng J, Xu L, Ma Q, Yang M, Fang Y, Wan G, Li R, Yuan J, Zhang X, Yu H, Liu L, Liu T (2022) Modulating crystal and interfacial properties by W-gradient doping for highly stable and long life Li-rich layered cathodes. Adv Func Mater 32(19):2113013

38. Song B, Zhou C, Wang H, Liu H, Liu Z, Lai MO, Lu L (2014) Advances in sustain stable voltage of Cr-doped Li-rich layered cathodes for lithium ion batteries. J Electrochem Soc 161(10): A1723–A1730

39. Liu FL, Zhang S, Deng C, Wu Q, Zhang M, Meng FL, Gao H, Sun YH (2012) Cobalt content optimization of layered $0.6Li[Li_{1/3}Mn_{2/3}]O_2–0.4LiNi_{0.5-x}Mn_{0.5-x}Co_{2x}O_2$ ($0 \le x \le 0.5$) cathode materials prepared by the carbonate coprecipitation. J Electrochem Soc 159(10):A1591-A1597

40. Ohzuku T, Ueda A, Nagayama M (1993) Electrochemistry and structural chemistry of $LiNiO_2$ (R3m) for 4 volt secondary lithium cells. J Electrochem Soc 140(7):1862–1870

41. Ohzuku T, Ueda A, Nagayama M, Iwakoshi Y, Komori H (1993) Comparative study of $LiCoO_2$, $LiNi_{1/2}Co_{1/2}O_2$ and $LiNiO_2$ for 4 volt secondary lithium cells. Electrochim Acta 38(9):1159–1167

42. Zhao C, Kang W, Liu R, Shen Q (2013) Influence of cobalt content on the electrochemical properties of sheet-like $0.5Li_2MnO_3·0.5LiNi_{1/3+x}Co_{1/3-2x}Mn_{1/3+x}O_2$ as lithium ion battery cathodes. RSC Adv 3(7):2362

43. Shen S, Hong Y, Zhu F, Cao Z, Li Y, Ke F, Fan J, Zhou L, Wu L, Dai P, Cai M, Huang L, Zhou Z, Li J, Wu Q, Sun S (2018) Tuning electrochemical properties of Li-rich layered oxide cathodes by adjusting Co/Ni ratios and mechanism investigation using in situ X-ray diffraction and online continuous flow differential electrochemical mass spectrometry. ACS Appl Mater Interfaces 10(15):12666–12677

44. Wu Y, Xie L, He X, Zhuo L, Wang L, Ming J (2018) Electrochemical activation, voltage decay and hysteresis of Li-rich layered cathode probed by various cobalt content. Electrochim Acta 265:115–120

45. Liu P, Zhang H, He W, Xiong T, Cheng Y, Xie Q, Ma Y, Zheng H, Wang L, Zhu Z-Z, Peng Y, Mai L, Peng DL (2019) Lithium deficiencies engineering in Li-rich layered oxide $Li_{1.098}Mn_{0.533}Ni_{0.113}Co_{0.138}O_2$ for high-stability cathode. J Am Chem Soc 141(27):10876–10882

46. Ma Q, Yin S, Ding F, Meng J, Zhong S, Dai C (2019) Understanding effects of lithium content on structural and electrochemical

characteristics of $Li_{1+x}Mn_{0.7}Ni_{0.2}Co_{0.1}O_{2.25+x/2}$ cathode materials for lithium-ion batteries. Mater Sci Eng B 246:143–152

47. Wang D, Wu Z, Xiang W, Liu Y, Wang G, Hu K, Xu Q, Song Y, Guo X (2022) Is it universal that the layered-spinel structure can improve electrochemical performance?, Journal of Energy. Chemistry 64:344–353

48. Pang S, Wang Y, Chen T, Shen X, Xi X, Liao D (2016) The effect of AlF3 modification on the physicochemical and electrochemical properties of Li-rich layered oxide. Ceram Int 42(4):5397–5402

49. Dong P, Wang D, Yao Y, Li X, Zhang Y, Ru J, Ren T (2017) Stabilizing interface layer of $LiNi_{0.5}Co_{0.2}Mn_{0.3}O_2$ cathode materials under high voltage using p-toluenesulfonyl isocyanate as film forming additive. J Power Sour 344:111–118

50. Ma Q, Wang Y, Lai F, Meng J, Dmytro S, Zhou L, Yang M, Zhang Q, Zhong S (2022) Induction and maintenance of local structural durability for high-energy nickel-rich layered oxides. Small Methods 6(6):2200255